Investigation of heavy-ion particle identification in an experiment to determine the astrophysical rate of $^{15}O(\alpha, \gamma)^{19}$ Ne via the ^{21} Ne(p,t) ^{19}Ne reaction

by

Amhimmid Ahfaaf

A THESIS SUBMITTED IN PARTIAL FULFILMENT OF
THE REQUIREMENTS FOR THE DEGREE OF

BACHELOR OF SCIENCE

in

Honours Astrophysics

(Department of Astronomy and Physics, Dr.Greg Christian supervising faculty)

.....
.....
.....
.....
.....

SAINT MARY'S UNIVERSITY

April 5, 2023

Abstract

Investigation of Heavy-Ion Particle Identification in an Experiment to Determine the Astrophysical Rate of $^{15}O(\alpha,\gamma)^{19}Ne$ via the $^{21}Ne(p,t)^{19}Ne$ Reaction

by *Amhimmid Ahfaaf*

submitted on April 5, 2023:

This study aims to investigate the heavy-ion particle identification in an experiment designed to determine the astrophysical rate of the $^{15}O(\alpha,\gamma)^{19}Ne$ reaction.

The $^{15}O(\alpha,\gamma)^{19}Ne$ reaction is one of two recognized pathways for breakout from the hot CNO cycle into the rp-process, which consists of consecutive proton captures onto seed nuclei to produce heavier elements. Understanding this reaction is crucial for elucidating the dynamics of X-ray bursts. To measure the branching ratios of α and γ decays, which determine the reaction rate of $^{15}O(\alpha,\gamma)$. The experiment involves populating excited states in ^{19}Ne using the $^{21}Ne(p, t)^{19}Ne$ reaction. In this study, we measure the decay branching ratios of excited states in ^{19}Ne by passing the decay products through a magnetic dipole and a set of Phoswich detectors. These detectors are capable of detecting heavy-ions. For obtaining accurate data on reaction rates and branching ratios, it is essential to accurately identify heavy-ion particles. This research aims to advance our knowledge of the nucleosynthesis of

heavy elements and offer important insights into the fundamental processes governing the behaviour of atomic nuclei by demonstrating conclusive isotope separation and identification in the phoswich detectors.

Contents

List of Figures

List of Tables

Chapter 1

INTRODUCTION

"Neutron stars are interesting objects not just for astrophysics, but for fundamental physics," Weinberg said. "At these very high densities—densities higher than the nucleus of an atom—we don't actually know how matter behaves." (Steven Weinberg, n.d. as cited in physics.org)

Neutron stars are intriguing objects for fundamental physics as well as astrophysics; they are created when a massive star explodes in a supernova and the remnants condense and collapse upon themselves as a result of extremely strong gravitation. Because of how tightly this material is compressed, neutron stars are formed when protons and electrons combine to form neutrons. If the neutron star and another star are in a binary system, the neutron star can draw material rich in hydrogen or helium from the other star, which then forms a thin layer on its surface. This layer ignites in a thermonuclear explosion when the neutron star reaches critical mass, pressure and temperature in this layer exceed a certain threshold, heating the entire surface to tens of millions of degrees Kelvin and causing an unexpected burst of X-rays.

Arguably, X-ray bursts are one of the many fascinating and exciting astronomical phenomena. They can last anywhere from hours to days, during which the emission from the star can increase by a factor of a million or more. This makes them crucial

to study in order to comprehend the total energy of these systems. In addition, X-ray bursts provide a deeper understanding of the universe's evolution and composition, allowing us to better comprehend the processes that shape the cosmos [2].

Despite ongoing research into the theoretical models of X-ray bursts, the dynamics of these bursts remain complex and many aspects of the mechanisms that drive them are still not well understood. Nevertheless, the study of X-ray bursts continues to be an exciting and important field in astrophysics. It has been extensively discussed how essential it is to understand X-ray bursts as a probe of neutron star characteristics and the underlying physics, with the potential to shed light on a range of fundamental questions in nuclear physics and the evolution of stars [6].

In this study, we focus on thermonuclear (type-I) X-ray bursts, which are triggered by unstable ignition of accreted fuel on the surface of neutron stars. These bursts are fundamental to comprehending the astrophysical processes that result in the formation of heavy-ion particles. It is important to note that the dynamics of type-I X-ray bursts are sensitive to the rates of the constituent nuclear reactions, promoting investigations of important reactions such as $^{15}\mathrm{O}(\alpha,\gamma)$ [2]. This sensitivity establishes an observable connection between nuclear physics and astrophysics, enabling a deeper understanding of the interplay between these processes. Therefore, examining thermonuclear X-ray bursts in this experiment is motivated by their potential to provide insights into the mechanisms underlying these bursts and their impact on nuclear reaction rates.

The dynamics of X-ray bursts are complex, and many aspects of the mechanisms that cause them are still poorly understood. However, understanding astrophysical

systems and the behaviour of matter in these analogous conditions depends on both types of X-ray bursts. It is worth noting that while thermonuclear fusion is well understood, the rates of specific constituent reactions are not sufficiently well-constrained. Through this investigation, we can gain insight into the composition and properties of the burning material, the burning behavior and ignition conditions, and the impact of the bursts on the neutron star's atmosphere and surface. This study of X-ray bursts is important for understanding the formation of heavy elements in the universe, providing a deeper understanding of the universe's evolution and composition.

1.1 Astrophysical rate of $^{15}O(\alpha,\gamma)^{19}Ne$

One of the key reasons why this study is important is that it can help shed light on the mechanisms responsible for the nucleosynthesis of heavy elements in the universe. The rp-process, which is responsible for the production of heavier elements in stars through a series of consecutive proton captures onto seed nuclei, is facilitated by breakout reactions from the hot CNO cycle. Three reactions potentially important for the breakout have been identified, namely $^{15}O(\alpha,\gamma)^{19}Ne$, $^{18}F(p,\gamma)^{19}Ne$, and $^{18}Ne(\alpha,p)^{21}Na$ [3]. In this thesis, the focus is on the measurement of the $^{15}O(\alpha,\gamma)^{19}Ne$ reaction via the ^{21}Ne(p, t). The $^{15}O(\alpha,\gamma)^{19}Ne$ reaction is a critical pathway for breakout from the hot CNO cycles into the rp-process, which ultimately leads to the creation of heavier elements in stars.Understanding the mechanisms of nucleosynthesis in the rp-process is essential for building a comprehensive understanding of the origin of the elements in our galaxy. This knowledge contributes to a broader perspective on the evolution of

stars and the formation of various elements, allowing us to piece together the complex processes that have shaped the composition of our universe.

1.1.1 Branching Ratio

The thermonuclear rate of the ^{15}O(α,γ) reaction is influenced by the branching ratios of resonance states through which the reaction proceeds. In resonant capture reactions, the total thermonuclear reaction rate can be expressed as the sum of individual resonance contributions, as described by equation 1.1 from Christian Iliadis' book "Nuclear Physics of Stars" [1]:

$$N_A\langle\sigma v\rangle = \frac{1.5399 \times 10^{11}}{(M_0 M_1/(M_0+M_1))T_9^{3/2}} \sum_i (\omega\gamma)_i e^{-11.605\frac{E_i}{T_9}} \tag{1.1}$$

where, N_A is Avogadro's number, M_1 and M_0 are the masses of the interacting particles, T_9 is the temperature in 10^9 degrees Kelvin, and $(\omega\gamma)_i$ is the resonance strength for each resonance level i. We have the following equation for the ^{15}O(α,γ) reaction:

$$\omega\gamma = \frac{(2J+1)}{(2J_1+1)(2J_2+1)} \frac{\Gamma_\gamma \Gamma_\alpha}{\Gamma_\gamma + \Gamma_\alpha} \tag{1.2}$$

This equation represents the resonance strength in the context of the ^{15}O(α,γ) reaction, taking into account the partial widths of γ and α transitions. Where J is the spin of resonance, J_1 is the spin of ^{15}O and J_2 is the spin of the α particle. Γ_α and Γ_γ are the widths of the gamma-ray and alpha decay.

Because $\Gamma_\alpha \ll \Gamma_\gamma$ for the state at an excitation energy of 4.03 MeV, we can

approximate the second term in the resonance strength as:

$$\frac{\Gamma_\gamma \Gamma_\alpha}{\Gamma_\gamma + \Gamma_\alpha} \approx \frac{\Gamma_\gamma \Gamma_\alpha}{\Gamma_\gamma} = \Gamma_\alpha \tag{1.3}$$

The branching ratio for alpha decay is given by:

$$\text{Branching Ratio} = \frac{\Gamma_\alpha}{\Gamma} \tag{1.4}$$

Therefore, $\omega\gamma = \omega\Gamma_\alpha$. To determine the branching ratios, we can find the partial alpha decay width Γ_α from a equation 1.4 combined with the known value of Γ_γ. The ^{21}Ne(p, t)^{19}Ne reaction is a powerful tool for studying the ^{15}O(α,γ) reaction because it preferentially populates the key resonance state at $E_x = 4.03$ MeV in ^{19}Ne, allowing scientists to determine the rate of the ^{15}O(α,γ)^{19}Ne reaction.

The reaction populates excited states in ^{19}Ne, and the branching ratio measurement is performed by passing the decay products through a magnetic dipole, followed by a set of Phoswich detectors will be utilized in this experiment to measure heavy ions, which are nuclei heavier than alpha particles. These detectors play a role in separating heavy ions reaching the focal plane based on energy loss and total energy.

1.2 PREVIOUS EXPERIMENTS DISCUSSION

1.2.1 THE ASTROPHYSICAL RATE OF $^{15}O(\alpha,\gamma)^{19}Ne$ VIA THE (P,T) REACTION IN INVERSE KINEMATICS BY B. DAVIDS ET AL.

Considering previous research on the astrophysical rate of the $^{15}O(\alpha,\gamma)^{19}Ne$ reaction, it is essential to investigate the α-decay branching ratios for the states in ^{19}Ne that lie just above the α-emission threshold of 3.529 MeV. These states, which can only decay by the emission of α particles or γ rays, play a crucial role in determining the reaction rate.

Historically, the α-decay branching ratios for these states were measured by populating them in transfer reactions and counting α particles or both α particles and ^{15}O nuclei [8] from the subsequent decays. While these studies provided useful information on higher-lying states, none yielded valuable data on the 3/2+ level at 4.033 MeV, which dominates the $^{15}O(\alpha,\ \gamma)^{19}Ne$ reaction rate at temperatures found, for example, in novae and type-I X-ray bursts. Prior to this discovery, the only experimental data on this state's contribution came from measurements of transfer processes that populated the analogue state in the mirror nucleus ^{19}F.

1.2.2 EXPERIMENT

B.Davids et al assessed the α-decay branching ratios of all ^{19}Ne states important to the astrophysical rate of the $^{15}O(\alpha,\ \gamma)^{19}Ne$ reaction. This measurement was conducted at the Kernfysisch Versneller Instituut (KVI) via the recoil coincidence method. In a

magnetic spectrometer, B. Davids et al. successfully distinguished the recoils resulting from both α- and γ-decay with 100% geometric efficiency. The variable energy, superconducting cyclotron AGOR bombarded a 1 mg cm^{-2} $(CH_2)_n$ target with a 910 MeV ^{21}Ne beam. The Big-Bite Spectrometer (BBS), set at 0°, was able to take in both triton ejectiles and ^{19}Ne recoils. The ^{19}Ne recoils are formed in the (p,t) reaction at the target position and immediately deexcited by either the emission of α particles, leading to the formation of ^{15}O decay products, or by the emission of γ rays, preserving their identities as ^{19}Ne. Using the p(^{21}Ne,t)^{19}Ne reaction with an incident beam energy of 910 MeV, this experiment filled states in ^{19}Ne. Figure 1.1 schematically illustrates the experimental arrangement.

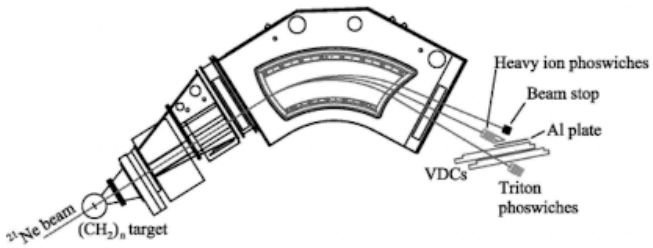

Figure 1.1: Schematic setup of this experiment is shown (not to scale for better presentation).

In two phoswich detectors [9] set up in a vacuum chamber similarly to the present experiment, the ^{19}Ne recoils and ^{15}O decay products were stopped and measaured. Information on energy loss, total energy, and timing was provided by these photoswitches.A 1 mm layer of fast plastic scintillator (NE102A) and a 5 cm layer of slow plastic scintillator (NE115) make up each detector. The various scintillators used in this experiment will be explained in Section 2.2, which focuses on the Phoswich

detectors.

A difficulty encountered in this experiment was that the cross section for fragmentation of the ^{21}Ne beam on the target, particularly due to the carbon nuclei in the target, was much larger than that for the (p, t) reaction. This means that when the ^{21}Ne ions hit the target, they tended to break apart into smaller fragments rather than undergo the desired nuclear reaction with the target protons. This resulted in a large background signal of fragmentation products, which made it difficult to detect the much smaller signal from the (p,t) reaction.

To address the issue of the unreacted beam, the experimenter used a Faraday cup to stop the ^{21}Ne beam just in front of an aluminum plate that was positioned behind the detectors. The Faraday cup is a device used to measure the charge of a beam of charged particles by collecting the particles on a conductive surface. In this case, the Faraday cup was used to stop the unreacted ^{21}Ne ions before they could reach the detectors, helping to reduce the background signal from the unreacted beam particles. However, the fragmentation issue remained, and the aluminum plate was used to help shield the detectors from the heavy fragmentation products, which tended to be deflected more strongly by magnetic fields than the (p,t) reaction products.

1.2.3 RESULTS

In addition to the measurements of heavy ions, the experiment also involves the detection of tritons, which are a part of the ^{21}Ne(p, t)^{19}Ne reaction. The relationship between triton scattering angle and kinetic energy is an important aspect of this study.

These quantities are depicted in a scatter plot in Fig 1.2 for ^{19}Ne-triton coincidence events, and in Fig 1.3 for ^{15}O-triton coincidences. The ^{19}Ne states represented by the curved loci in these illustrations have excitation energies that rise as triton kinetic energy rises.

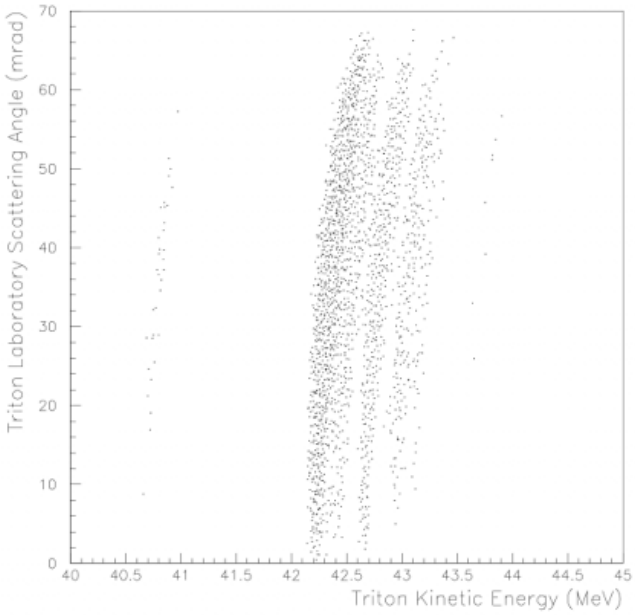

Figure 1.2: Triton laboratory scattering angle plotted against kinetic energy derived from ^{19}Ne-triton coincidences. The curved loci show γ decays of ^{19}Ne states.

The experimenters fit the resulting spectra from coincidence spectroscopy measurements with multiple Gaussian functions, as shown in Fig 1.4. The resolution was not precise enough to distinguish between some closely-spaced energy levels, so the yield for each level was estimated from the Gaussian fits. However, some energy levels, such as the 4.033 MeV and 4.379 MeV states, were well-resolved. This resolution allowed for a reliable extraction of their cross-sections and subsequently the gamma-decay probability of these states, which is importnat step for understanding

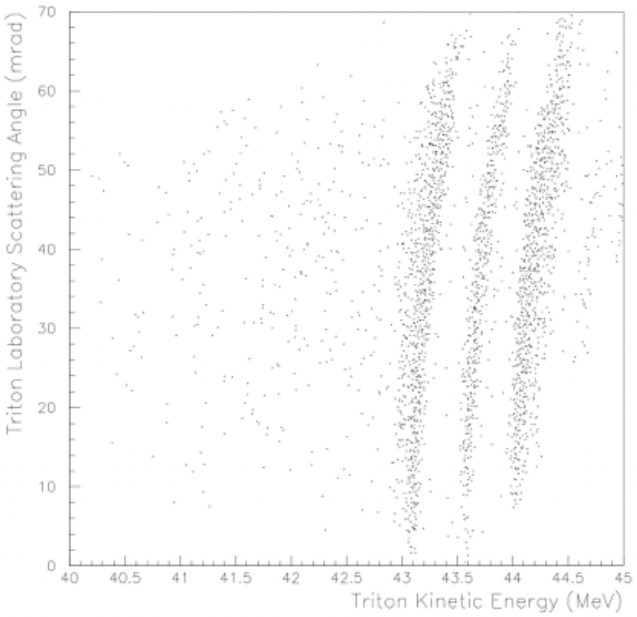

Figure 1.3: kinetic energy from ^{15}0-triton coincidences as a function of triton laboratory scattering angle, in logarithmic scale. The curving loci show the decay of states in ^{19} Ne.

the astrophysical reaction rate in novae. The 4.033 MeV state was populated by an s-wave transfer of two neutrons from the 3/2+ ground state of the ^{21}Ne beam to the proton target. This inference of the s-wave transfer comes from a much earlier study of ^{21}Ne(p,t) [4].

In addition to the spectrum shown in Fig 1.4, Fig 1.5 displays a similar excitation energy spectrum in coincidence with ^{15}O recoils, which are the result of alpha decays. The experiment involved ^{21}Ne ions colliding with carbon nuclei in a $(CH_2)_n$ target, producing ^{15}O and tritons. For the four highest-lying states with excitation energies of 4.549, 4.600, 4.712, and 5.092 MeV, the experimenters were able to determine the branching ratios of the alpha decay through fitting the data. The peaks in Fig 1.5 were fit with Gaussians, and then the total number of counts in each peak was divided by the number of counts in the corresponding gamma-gated peak from Fig 1.4 to

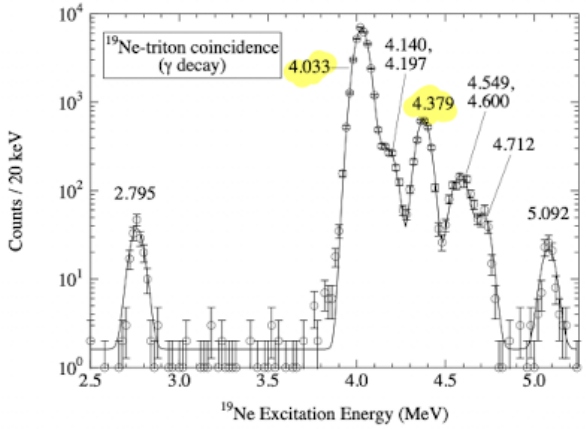

Figure 1.4: The excitation energy spectrum of ^{19}Ne, reconstructed from tritons in coincidence with ^{19}Ne, represents the gamma decays of ^{19}Ne states. No detected gamma decays of states higher than 5.092 MeV were observed.

determine the branching ratio. This is because the ratio of counts in Fig 1.5 to Fig 1.4 is equivalent to $\Gamma\alpha/\Gamma\gamma$. The experimenters were unable to observe alpha decay from the 4.140 MeV and 4.197 MeV states and could not determine the alpha-decay branching ratios for these states.

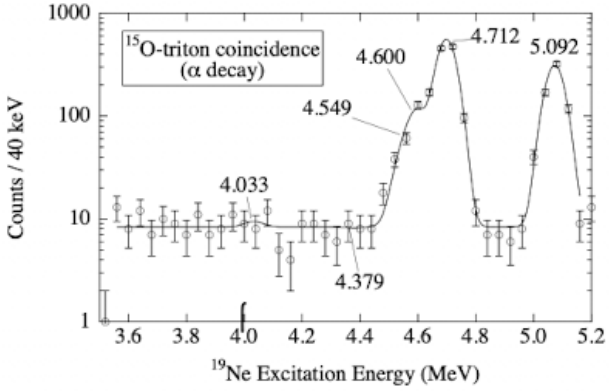

Figure 1.5: The region of astrophysical interest is highlighted in the logarithmic scale ^{19}Ne excitation energy spectrum obtained from ^{15}O triton coincidences. Six Gaussians corresponding to known states in ^{19}Ne, whose widths were set by the experimental resolution, are added to a constant background to create the curve.

The researchers used a Bayesian statistical analysis to obtain upper limits on the

alpha-decay branching ratios of two states located at 4.033 MeV and 4.379 MeV. The upper limits set a constraint on the probability of the states decaying by alpha emission. Table 1.1 shows the measured branching ratios of B.Davids et al and other studies, including the central values, uncertainties, and upper limits. The passage also notes that no evidence for gamma decay of states above 5.092 MeV was observed, and the observation of alpha decay from states at 5.424-, 5.539-, and 5.832 MeV is consistent with 100% alpha-decay branching ratios for these states.

Table 1.1: decay widths and branching ratios $B_\alpha = \Gamma_\alpha/\Gamma$. Maximum values are given at a 90% level of confidence.

E_x (MeV)	J^π	B_α(B.davids et al work)	B_αRef. [10]	B_α Ref. [8]	B_α (adopted)	Γ_γ(meV)	Ref	Γ(meV)
4.033	$(3/2)^+$	$<4.3 \times 10^{-4}$			$<4.3 \times 10^{-4}$	45^{+200}_{-33}	[5]	< 0.13
4.379	$(7/2)^+$	$<3.9 \times 10^{-3}$	0.044 ± 0.032		$<3.9 \times 10^{-3}$	458 ± 92	[3]	< 2.3
4.549	$(3/2)^-$	0.16 ± 0.04	0.07 ± 0.03		0.10 ± 0.02	39^{+34}_{-15}	[15]	$4.4^{+4.0}_{-2.0}$
4.600	$(5/2)^+$	0.32 ± 0.04	0.25 ± 0.04	0.32 ± 0.03	0.30 ± 0.02	101 ± 55	[11]	43 ± 24
4.712	$(5/2)^-$	0.85 ± 0.04	0.82 ± 0.15		0.85 ± 0.04	43 ± 8	[15]	230 ± 80
5.092	$(5/2)^+$	0.90 ± 0.04	0.90 ± 0.09		0.90 ± 0.05	107 ± 17	[13]	960 ± 530

1.2.4 $^{15}O(\alpha,\gamma)^{19}Ne$ Breakout Reaction and Impact on X-Ray Bursts by Notre Dame (3He,t)

Another experiment studying the breakout reaction $^{15}O(\alpha,\gamma)^{19}Ne$ was performed using the $^{19}F(^3He,t)^{19}Ne$ reaction at Notre Dame. This reaction is essential for controlling the flow between the hot CNO cycle and the rp process. The critical alpha-decay branching ratios of the pertinent ^{19}Ne states were successfully measured, and the rate of $^{15}O(\alpha,\gamma)^{19}Ne$ was derived using lifetime measurements of these states [14].

1.2.5 EXPERIMENT

Figure 1.6 shows the experimental set-up that was used in the experiment. A 40 μm/cm^2 thick CaF_2 target mounted on a 20 μm/cm^2 thick carbon foil was the target of a 24 MeV ^{3}He beam that was produced at the University of Notre Dame's FN tandem accelerator. As a large-acceptance momentum separator, the TwinSol dual inline superconducting solenoid ion-optical system, was used to separate tritons from other reaction products. The solid angle that fit within the acceptance range was 50 msr. A large area position-sensitive Δ E-E telescope with two 500 μm thick silicon detectors was installed near the TwinSol focal plane to detect and track tritons.

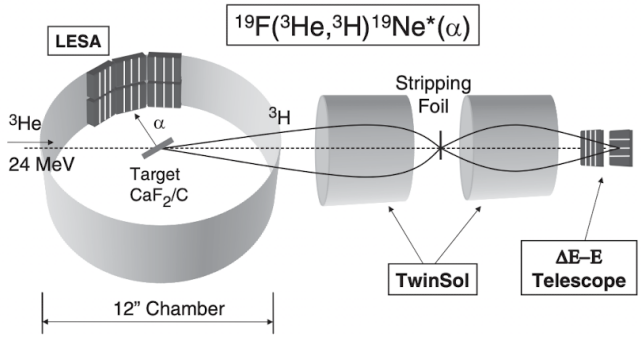

Figure 1.6: Schematic setup of this experiment is shown [14]

A Low Energy Silicon-strip Array (LESA) was created especially for this experiment in order to identify the low energy alpha particles generated by the decay of excited states in ^{19}Ne. Six identical silicon-pad detectors with a thickness of 300 μm each make up the LESA. Each one has an area of 4x4 cm^2 and four strips. The dead layer was kept to less than 0.05 μm in thickness to lower the detection threshold, which resulted in energy loss for 200 keV α particles of less than 14 keV being seen. The energy and time of flight of the particle from the target to LESA were measured

in order to identify the particle in LESA.

1.2.6 RESULTS

In Fig.1.7, the triton energy spectrum is displayed, highlighting the separation of the excited states in ^{19}Ne. However, there were some limitations due to double hits in the telescope which contributed to the background in the triton spectrum. In Fig. 1.8, the kinematically corrected α spectra for the decay of the observed ^{19}Ne states is presented. The left panels show the total and background α spectra, while the right panels show the net spectra after subtracting the background. The researchers found that while the α group for the decay of the 4.55-MeV state in ^{19}Ne was quite pronounced, weak α-decay branching ratios on the order of 10^{-3} or less were observed for the levels near the α threshold. Overall, the researchers were able to collect enough counts to ensure that the sensitivity of the measurements of α decay branching ratios reached as low as 10^{-4}.

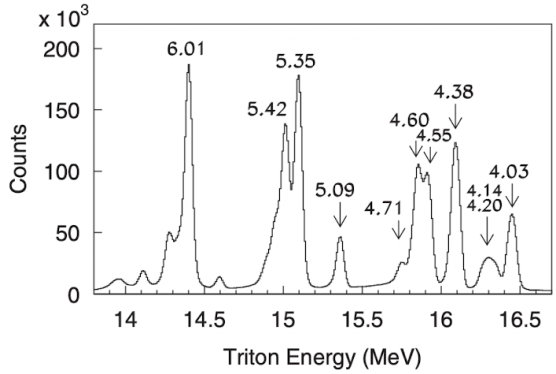

Figure 1.7: The ΔE-E particle identification method is used to display the total energy spectrum of tritons found in the telescope. Peaks in ^{19}Ne that are connected to excited states are marked.

The experiment has provided branching ratios for the first time for the states near

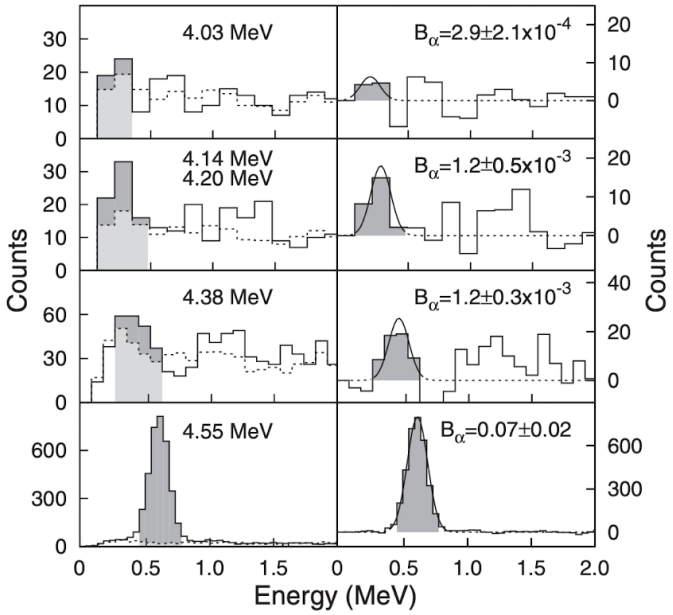

Figure 1.8: The ΔE-E particle identification method is used to display the total energy spectrum of tritons found in the telescope. Peaks in ^{19}Ne that are connected to excited states are marked.

the α threshold at 4.03-4.38 MeV. The 4.03-MeV state was found to have an α-decay branching ratio of 2.9 $\pm$ 2.1 x 10^{-4}, which is consistent with previous upper limits. The two states at 4.14 and 4.20 MeV were not resolved, but their combined branching ratio of 1.2 $\pm$ 0.5 x 10^{-3} was determined, which is surprisingly large compared to previous predictions. The measured α peak appears to be lower in energy than the simulated one, indicating that these decay events are more likely from the 4.14-MeV state. The 4.38-MeV state has a branching ratio of 1.2 $\pm$ 0.3 x 10^{-3}, which agrees with a stringent upper limit but differs from previously given values that were handicapped by poor statistics and lack of experimental resolutions. The states at higher excitation energies of 4.55-5.09 MeV show excellent agreement with previous results.

With the new experimental rate in hand, researchers can now better identify the ignition conditions of x-ray bursts and improve their understanding of the dynamics

and mechanisms behind these events. Prior to this study, simulations and calculations had established the transition point at $\dot{M} \sim 2.1$ x10^{18} g s^{-1} for a neutron star with R=10 km and M=1.4M$_\odot$ adopting a solar composition for the accreted matter. However, these previous findings did not take into account the uncertainty of the ^{15}O(α,γ)^{19}Ne reaction, which is now better constrained by the current experimental results.

With the new measurement, the authors were able to determine the transition point between steady state burning and unstable burning with significantly improved accuracy. They performed several calculations for different accretion rates, taking into account the luminosity resulting from the nuclear burning. They also performed identical calculations for the one sigma upper and lower limits of the reaction rate, which showed that the upper limit yields the same transition accretion rate, whereas the lower limit increases the transition point to $\dot{M} \approx 2.1$ x10^{18} g s^{-1} .

Further model studies of the transition accretion rate are necessary to better account for the mass and radius of the neutron star as well as the accreted composition. The authors emphasize the importance of laboratory results in providing stringent limits for burning conditions in stellar objects and demonstrate how experimental nuclear data can complement observational results and provide important insights for astrophysical model simulations. The ^{15}O(α,γ)^{19}Ne reaction is crucial for understanding the onset of x-ray bursts, and the experimental results bring us closer to a better understanding of the complex interplay between fuel supply and burning processes at the extreme conditions of the neutron star atmosphere.

Chapter 2

Setup and Procedure

2.1 SET UP

The experiment involves firing a beam of ^{21}Ne particles through a target made of $(CH_2)_n$ ("polypropelene" compound) which causes ^{21}Ne(p,t) reaction to occur as shown in Figure 2.1. This reaction results in the release of tritons, which are particles consisting of a proton and two neutrons, and the population of excited states in the nucleus of ^{19}Ne. And the experiment focuses on measuring the branching ratios of the different decay modes.

The heavy (beam-like) products pass through the Magnetic Mass Spectrometer (MDM), as described by Pringle et al in the NIM-A paper [12]. Both dipole and multipole magnets are used in the MDM spectrometer to bend the path of the charged particles as they pass through them. The momentum of the particle and the strength of the magnetic field both affect how the path bends. A multipole magnet is utilized to focus the isotopes after the reaction has occurred towards the dipole magnet, as shown in Figure 2.2.

The focal plane detectors consist of Phoswich detectors and Parallel Plate Avalanche Counters (PPACs). The Phoswich detectors are responsible for particle identification through ΔE-E measurements, while the PPACs provide position information for the

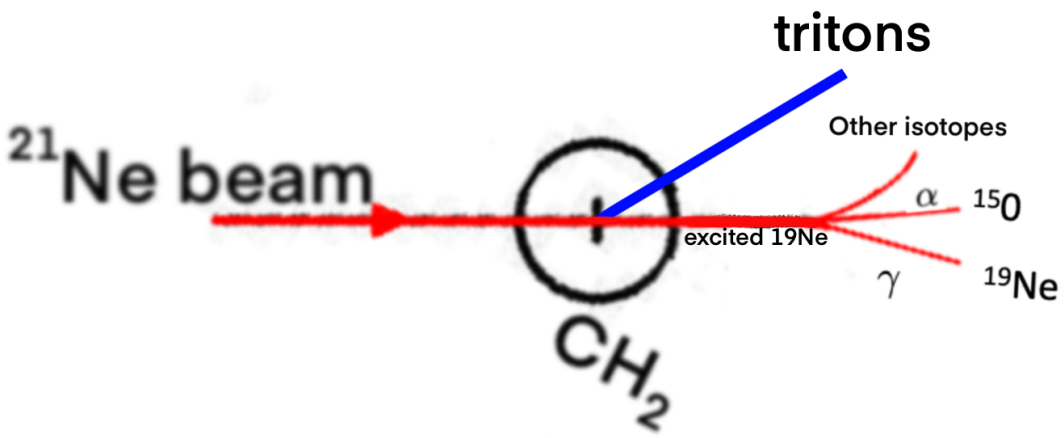

Figure 2.1: Schematic drawing ^{21}Ne(p,t) reaction

particles. With these detectors combined, the experiment is able to accurately identify and track the particles involved in the reactions under investigation.

The combination of the magnets, Phoswich detectors, and PPACs in the experimental setup allows for the identification and measurement of heavy ions produced in the ^{21}Ne(p,t) reaction, and the determination of their trajectory and energy deposition for accurate particle identification, which is necessary to determine the decay branching ratios of interest.

The configuration of valence protons in the excited state of the ^{19}Ne nucleus (excitation energy 4.03 MeV) is significant in the ^{21}Ne(p,t) reaction. The "two-hole"

configuration of the 4.03 MeV state makes the ^{21}Ne(p,t) reaction particularly useful, as the reaction removes two protons from the beam, leading to a high probability of populating two-hole states like the 4.03 MeV state.

The tritons are measured using a stack of four annular silicon detectors (3x 1.5 mm plus 1x 0.5 mm thickness) located 150 mm downstream of the target. By measuring the kinetic energy and scattering angle of these tritons, we can identify which states were populated in ^{19}Ne. A drawing of the experiment setup is shown in figure 2.2.

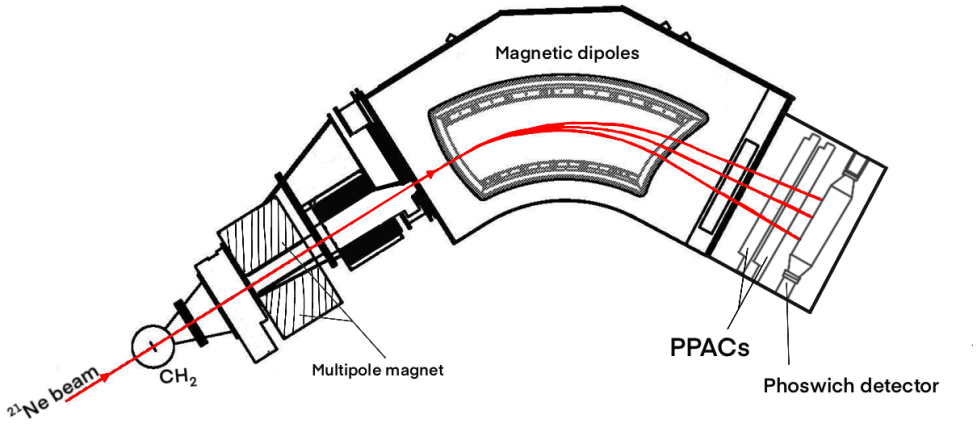

Figure 2.2: Schematic setup of this experiment is shown

2.2 Phoswich detectors

Figure 2.3 illustrates the composition of Phoswich detectors, which consist of two scintillators: a thin layer (1 mm) of EJ-262 and a thick layer (10 mm) of EJ-260. These scintillators measure the energy loss in their respective layers. The unique design of Phoswich detectors allows for the extraction of energy deposition information from both layers using a single signal. To achieve this, the detector uses "short" and "long" gates that allow the decoupling of signals from the two layers. As illustrated in Figure 2.4, the "short" and "long" signals don't exactly match up with the energy deposited in the thick and thin layers. The "long" gate measures the sum of the energy deposited in both the thick and thin layers, while the "short" gate measures the energy deposited in the thin layer.

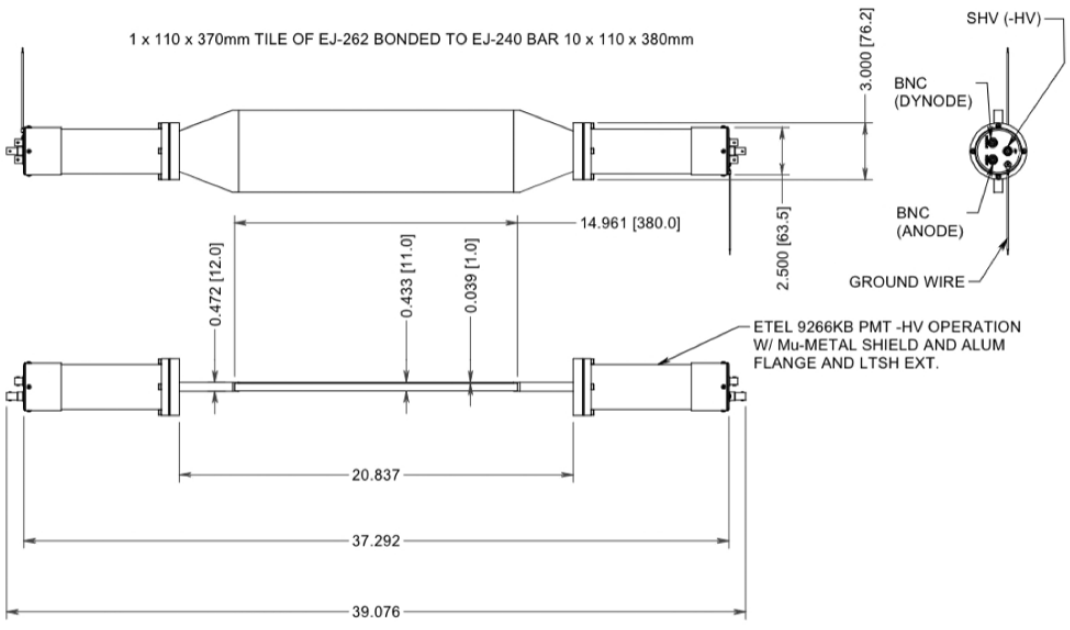

Figure 2.3: Schematic drawing of Phoswich detectors

The detector signals are calibrated using specific formulas to accurately identify

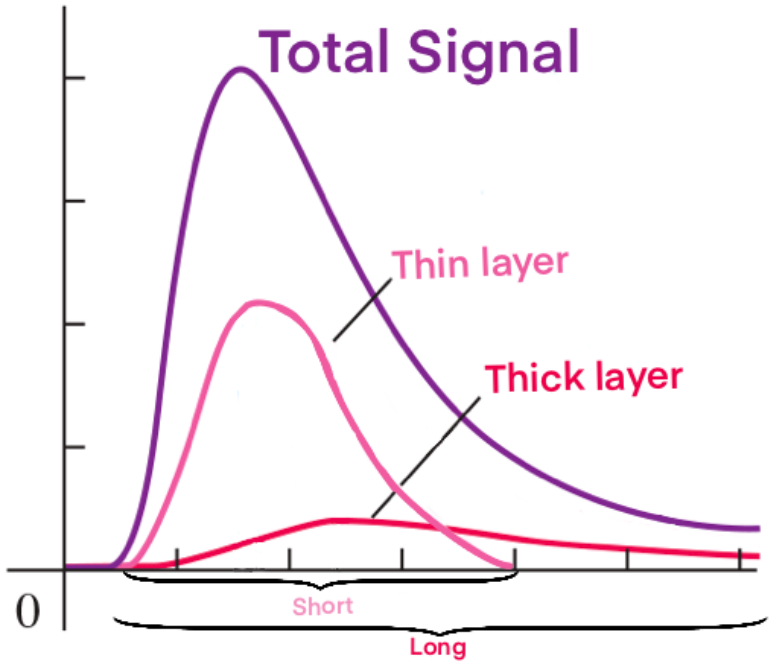

Figure 2.4: The Figure illustrates the discrepancy between the "short" and "long" signals and the actual energy deposition in the thick and thin layers of the phoswich detector.

particles based on the energy losses detected by the EJ-262 and EJ-260 scintillators. A detailed explanation of the calibration process, is provided in Section 3.1.2.

The experiment makes use of position-sensitive detectors known as Parallel Plate Avalanche Counters (PPACs) in addition to Phoswich detectors. PPACs are used to determine the trajectory and position of the ions making it through the MDM. The next section contains a thorough explanation of the PPACs.

The investigation of heavy-ion particle identification is an important step in determining the astrophysical rate of the $^{15}O(\alpha,\gamma)^{19}Ne$ reaction. Phoswich detectors can distinguish between different types of particles based on their energy loss in a 1 mm

layer of scintillator combined with their total energy, which can be used for identifying the produced particles. One example of particle identification using Phoswich detectors is the energy loss signal. The energy loss of charged particles passing through matter depends on the particle's atomic number, Z, and its velocity. According to the Bethe-Block equation [7], the energy loss is proportional to Z^2. Therefore, a heavier particle produces a stronger energy loss signal than a lighter particle, due to the Z^2 dependence of energy loss. This energy loss signal can be used to distinguish between different types of particles in heavy-ion experiments.

The light output of the two scintillators can be influenced by Z and A. As a result, the detectors' energy response needs to be calibrated to translate the raw electronic signals into meaningful physical values[9]. We will discuss this in more detail in the chapter on the calibration method.

2.2.1 PPAC Detectors

PPACs (Parallel Plate Avalanche Counters) work by holding two plates at a high voltage in a gas-filled chamber. Ionization of the gas by the passage of ions through the chamber will cause electrons to accelerate toward the plates, resulting in a cascade of secondary electrons.As a result, a signal that can be used to locate the ion inside the detector is produced. It is therefore possible to determine the ions' complete trajectory, including their position and angle in the x and y planes.

In this experiment, PPACs are equipped with Kapton exit windows that are 50 microns thick and 25 microns thick, respectively. The polyimide film Kapton is

renowned for its durability and resistance to extreme temperatures. Pentane gas is used to fill the space between the two Kapton windows; it has a density of 2.5x10^{-5} g/cm^3 and a thickness of 65 cm.

The anode is divided into numerous tiny pieces, each of which is connected to a delay line, in order to pinpoint the location of the ion. The electronic signal takes longer to get to the data acquisition electronics because of the delay line. The signal takes longer to be detected the further the ion is from one side of the detector. and The uncalibrated position spectrum, which can be used to locate the ion in the detector, is obtained by plotting the time difference between the anode and the cathode. Figure 2.5 shows a schematic drawing of the PPAC.

2.3 Methods used

In order to correctly identify the particles produced in the reaction, it is important to calibrate the detectors and correct for any position dependencies in the data. This is accomplished by calibrating the scintillators and PPACs to display position-corrected graphs, and adjusting the Phoswich for location dependencies and light collection techniques utilizing beam-centered data.

Once the detectors have been properly calibrated and corrected, the energy loss versus total energy plots can be used to identify the particles produced in the reaction. These plots are created for the production run and compared with estimated curves that correspond to the correct energy levels for various ion species. An ion-optical tracking code is used to generate these curves, which are then used to establish particle

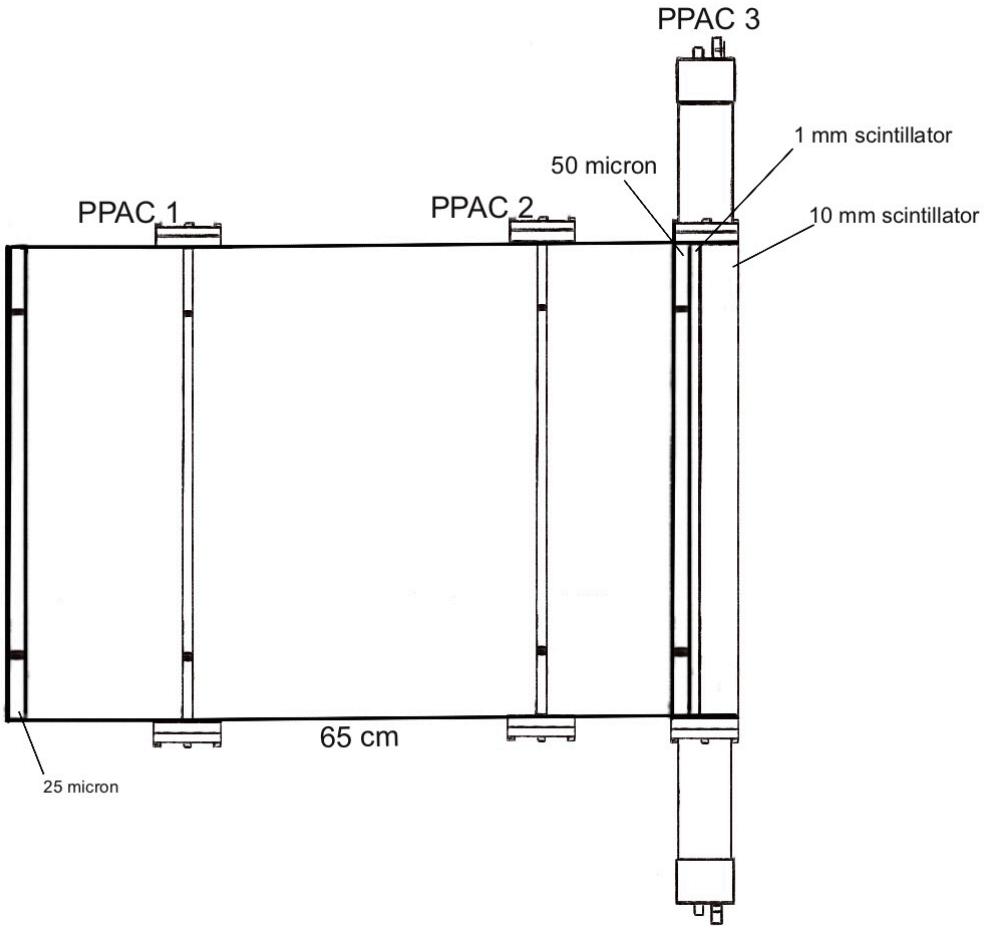

Figure 2.5: Schematic drawing of PPACs

identification.

Particle identification is a critical component of this experiment, as it allows us to determine the decay mode of the excited states in ^{19}Ne. The accurate identification of the particles produced in the reaction is essential for the interpretation of the experimental data and for the extraction of decay branching ratios for states in ^{19}Ne. By properly calibrating the detectors and utilizing energy loss versus total energy plots, particle identification can be achieved.

2.3.1 Root software

The ROOT software was used to perform the data analysis, including analyzing the raw data collected from the experiment and calibrating the PPACs position. The software allows C++ routines to be written to transform the data, creating event-by-event energy loss and position parameters for each ion passing through the detector. These can then be analyzed to identify the species of each particle passing through the detector

Also, the sophisticated graphics capabilities of ROOT made it possible to generate high-quality charts and figures to display the findings of the investigation. The software's flexibility and versatility allowed for easy customization and adaptation to the specific needs of the experiment.

Chapter 3

Analysis and Results

3.1 Detector Calibration

The experimental setup consisted of two detectors, PPAC 1 and PPAC 2, with a distance of 420mm between them. Each PPAC contained three small charge-collection gaps with a width of 1 mm at known positions, allowing for calibration in the dispersive (x) direction. The total detector size was 402 mm. The position of the particles hitting the detectors was indicated by dips in the uncalibrated graphs.

To accurately determine the position of the particles, the uncalibrated graphs (3.2 and 3.1) were analyzed, and the dips corresponding to the particles hitting the center of the detectors were identified, as shown in Table3.1. These dips, which are circled in Figures 3.1 and 3.2, allowed for the calibration of the detectors and the obtaining of precise measurements of the particles' position.

Gap position	position for PPAC 1	position for PPAC 2
-99.75 mm	2131	2090
0mm	5609	5656
99.75 mm	9068	9130

Table 3.1: This Table shows the actual Gap positions co-respond to the uncalibrated postions for PPAC 1 and PPAC 2

The actual positions of the PPACs dips were determined using the positions of the dips in the uncalibrated graphs. This was achieved by fitting a line to the locations of

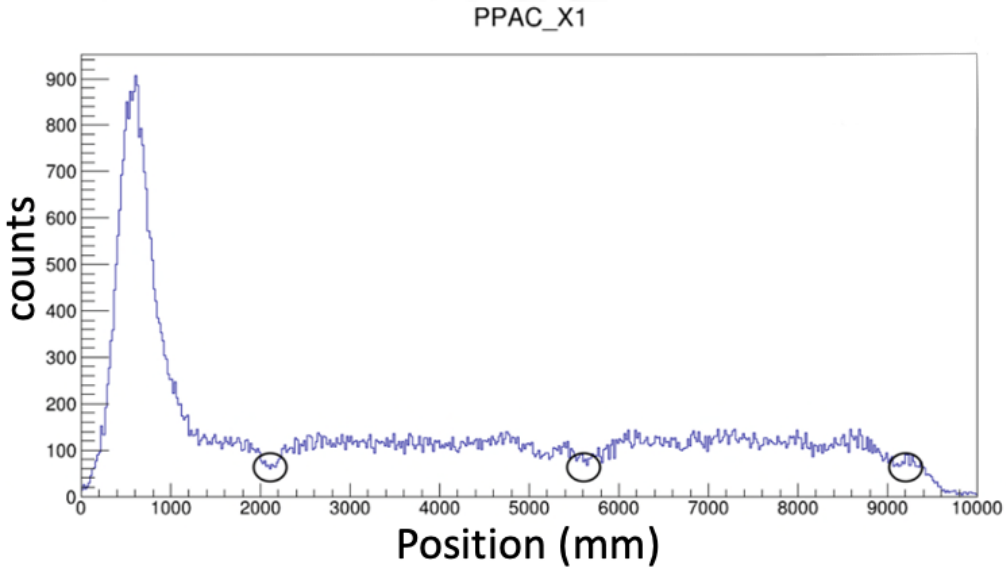

Figure 3.1: dips in the uncalibrated graphs for PPAC 1

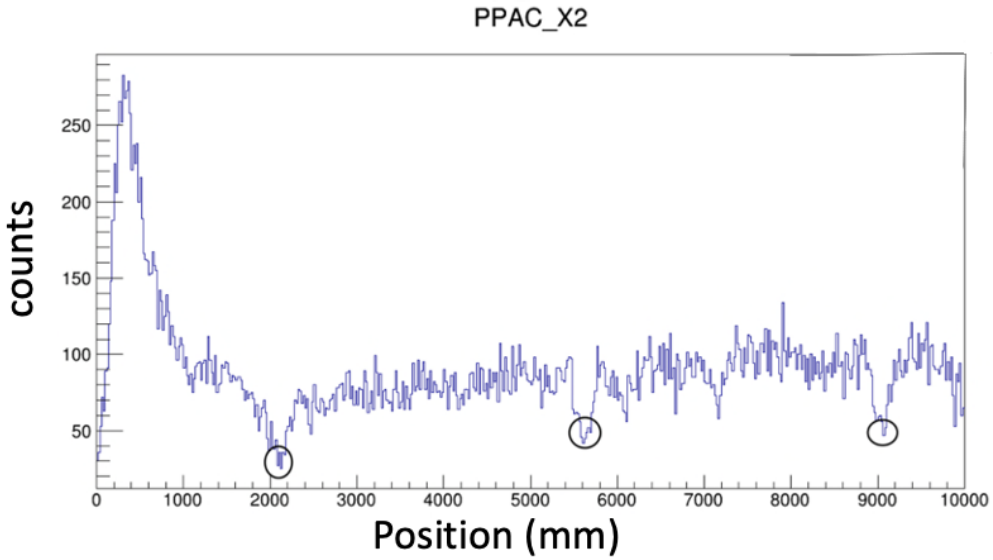

Figure 3.2: dips in the uncalibrated graphs for PPAC 2

the dips and using the slope and intercept to determine where the detectors were in relation to the source as seen in graph 3.3 and 3.4. The calibrated positions for PPAC 1 and PPAC 2 have been successfully determined through this process, as shown in figure 3.5.

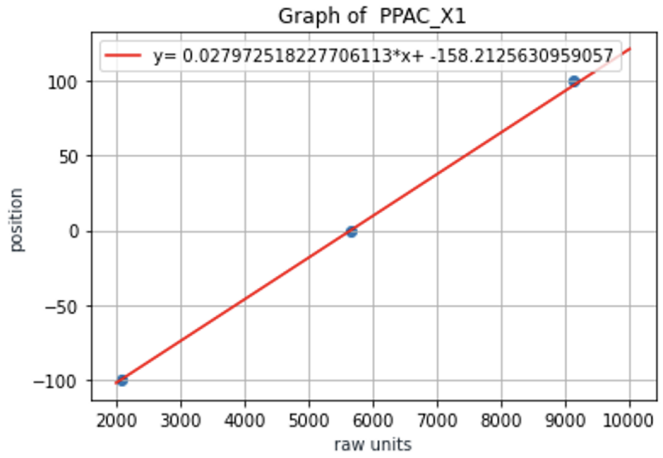

Figure 3.3: Fitted Line Plot for PPAC 1 Dips.

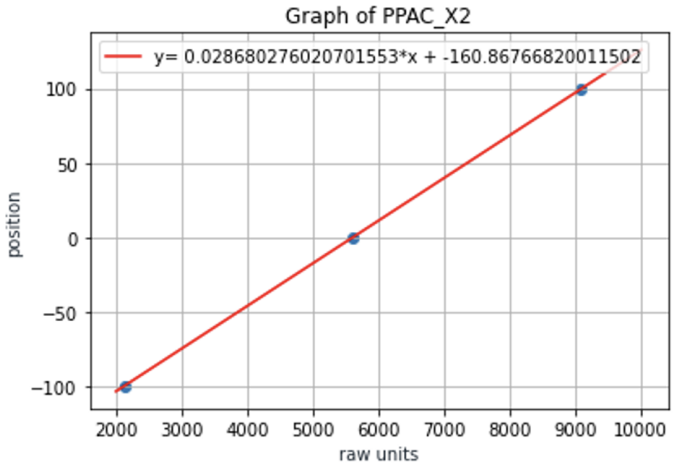

Figure 3.4: Fitted Line Plot for PPAC 2 Dips.

3.1.1 Virtual Position Calculations in Scintillators

After calculating the calibrated positions of the PPACs, the virtual position of the ions on the scintillator must be determined. In order to calculate the virtual position, one would use the positions of charged particles on the PPACs in conjunction with

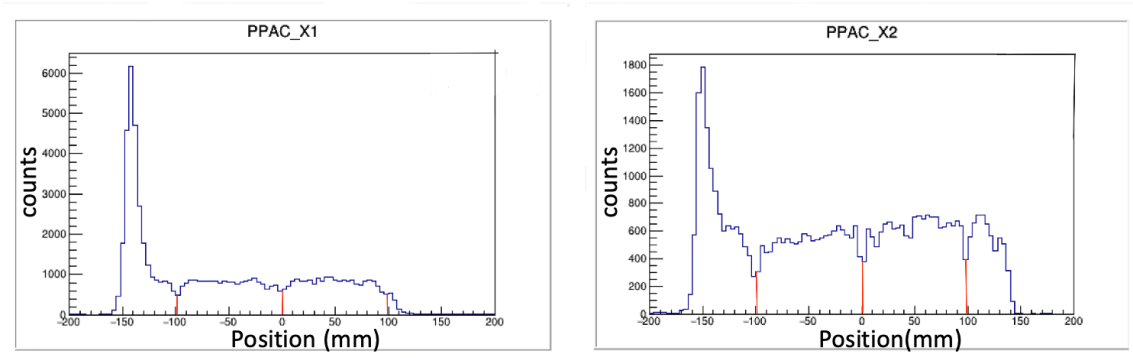

Figure 3.5: dips in the calibrated graphs for PPACs

the known geometry of the experiment setup shown in Figure 3.6 to determine the trajectory of the ions before they hit the scintillator.

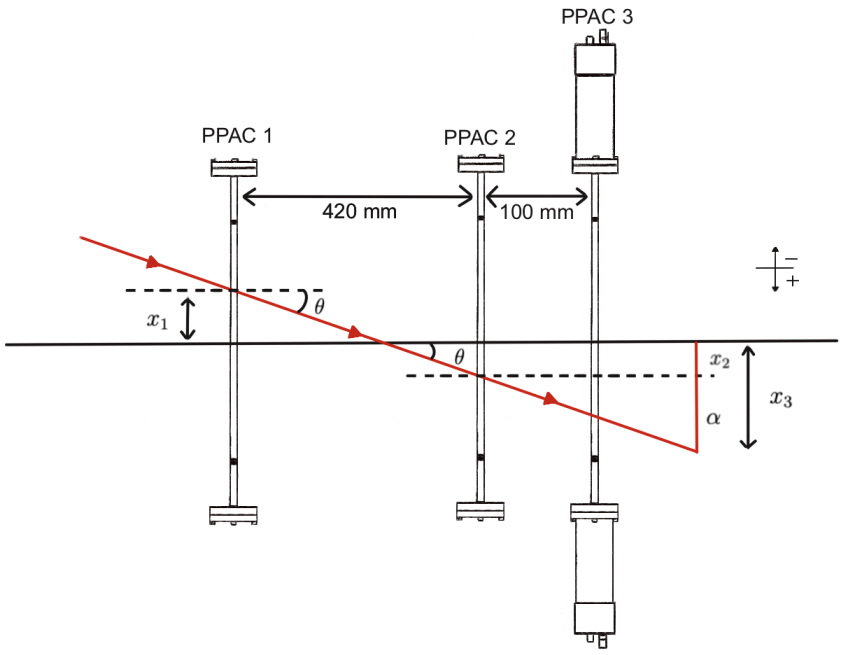

Figure 3.6: known experimental setup geometry

The equation 3.3 takes into account the geometry of the experimental setup and the trajectory of the ions before they hit the scintillator. It involves factors as the

distance between the PPACs and the scintillator.

$$\tan(\theta) = \frac{x_2 - x_1}{420} \tag{3.1}$$

$$\tan(\theta) = \frac{\alpha}{100} = \frac{x_3 - x_2}{100} \tag{3.2}$$

$$x_3 = \tan(\theta) \times 100 + x_2 \tag{3.3}$$

Equations (3.1, 3.2, and 3.3) derived from the geometry shown in figure 3.6 were used to determine the virtual position of scintillator. The equations were modified to represent the calibrated positions of PPAC1 and PPAC2. Using this technique, the virtual scintillator position was calculated, which allowed for the determination of the exact location where the ion made contact with the scintillator. This information was then used for the energy loss corrections, as seen in figure 3.7.

3.1.2 Calibration of Detector Signals and Particle Identification

In the past, the calibration method focused on matching the "residual energy," which is the energy remaining after passing through the thin (short) layer. However, it became evident that the "long" gate measurement actually represents the energy deposition in both the thick and thin layers, as it integrates the entire signal containing both components. To address this, we adopted new calibration formulas: Short =

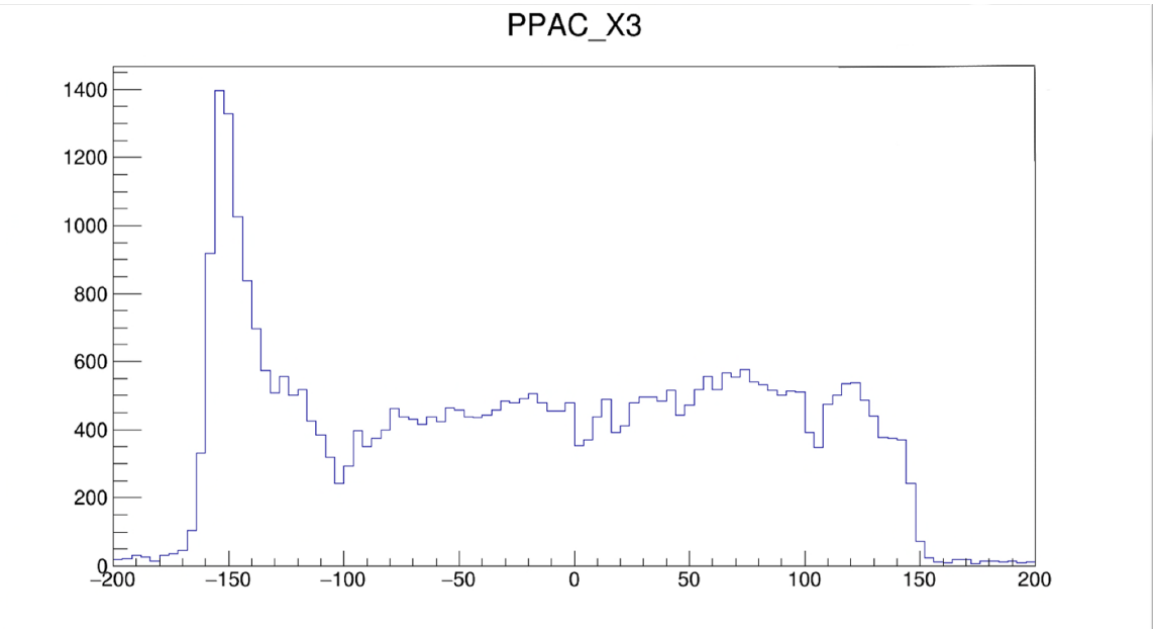

Figure 3.7: calibrated virtual position of the ions on the scintillator

Short + (F) * Long and Long = Long + Short. The variable F is a percentage value used for calibration, as illustrated in Figure 3.8. The optimal F value corresponds to the graph that best resembles the curvature of the isotopes under investigation.

3.1.3 Energy Loss Correction with Cubic Spline

When a beam of constant energy is scanned across the focal plane by varying the dipole field, the plot of energy deposited in the scintillators (both thin and thick layers) versus the particle's position on the scintillator (Phoswich xpos) is expected to be constant, as the energy and species of the incident ions remain the same. However, as shown in Fig. 3.9, this is not the case due to non-uniform light collection within the scintillator. To maximize the resolution of the energy loss and total energy signals, this position dependence needs to be corrected. Once the position dependency is accounted for in the energy loss formula, the resulting plots of energy loss in the thin

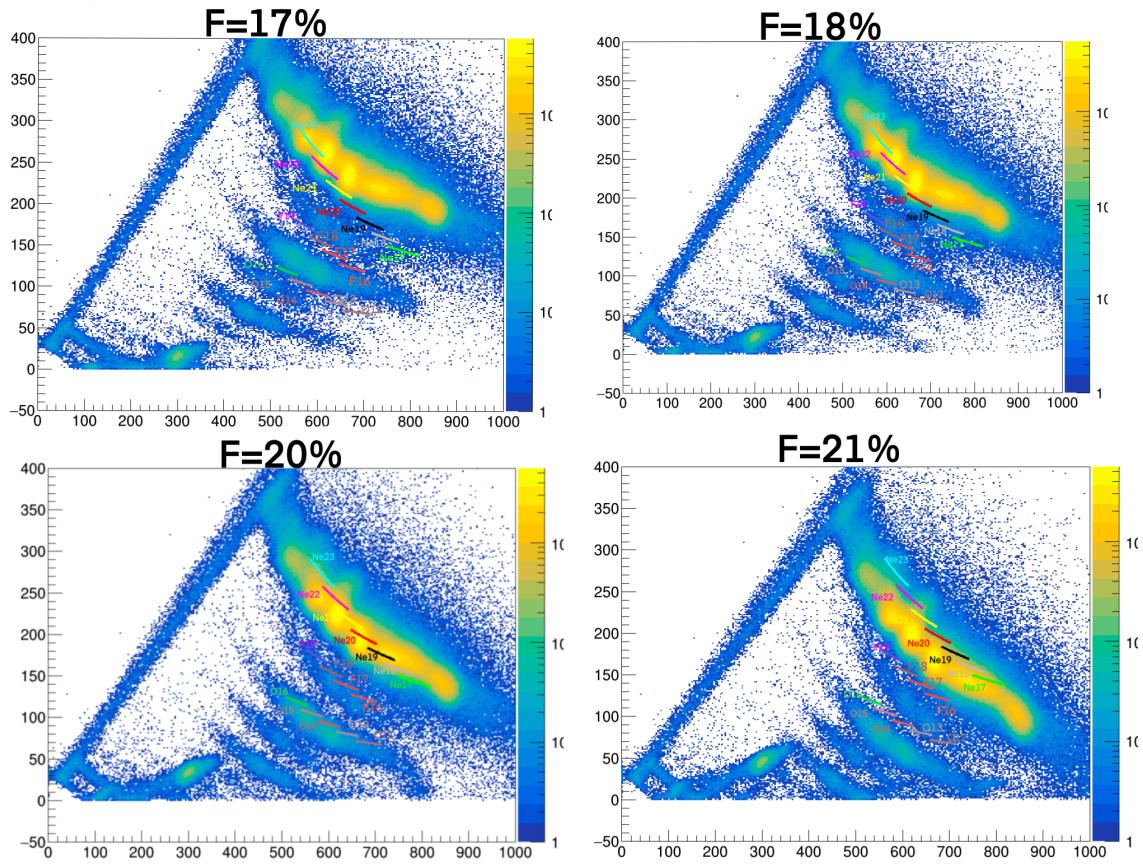

Figure 3.8: The lines represent the positions of the isotopes with different calibration graphs with various F values.

layer (Phoswich eshort) and energy loss in the thick layer (Phoswich elong) versus Phoswich xpos may still exhibit substantial variation due to the position dependence.

To obtain the corrected position dependency in energy loss signals, the cubic polynomials method is used for correcting position dependence. The first step is to obtain a set of calibration data points by measuring the elong and eshort signals at positions along the scintillator surface. When the data is collected, a cubic spline curve is fitted to the data using Root software, as shown in Figure 3.9.

After the cubic spline curve has been obtained we getcorrected energy vs. position as shown in fig 3.10, then it can be used to correct the position dependence in the

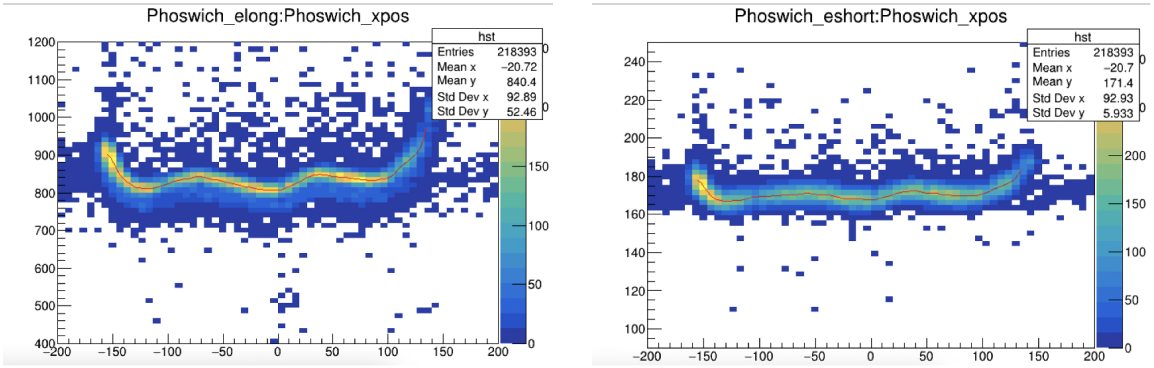

Figure 3.9: Phoswich_elong and Phoswich_eshort versus Phoswich_xpos using cubic spline method.

energy loss signals by interpolating the values of Elong and Eshort at any position along the scintillator. This corrected data can then be plotted against the position of the charged particle on the scintillator to obtain a position-corrected graph.

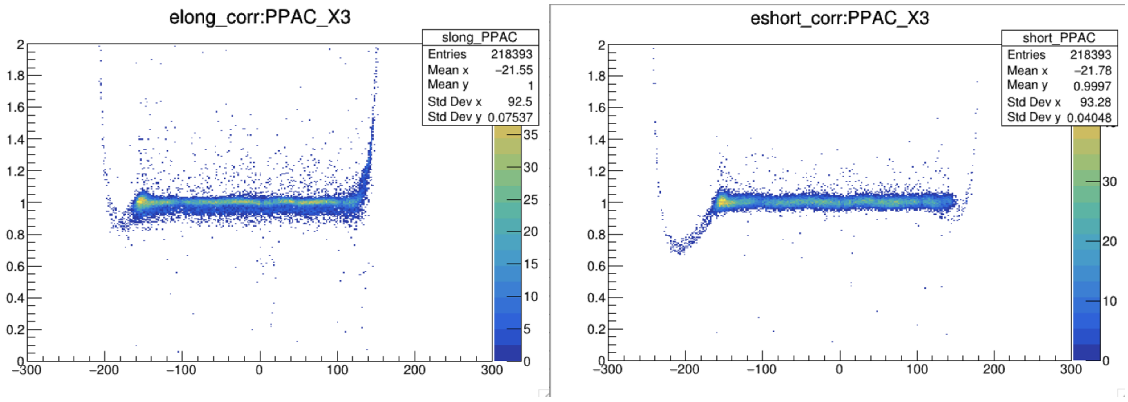

Figure 3.10: corrected energy vs. position

The resulting position-corrected graph will show much less variation due to position dependence, allowing for more accurate measurements of the true energy loss signals as shown in the figure 3.11 which shows corrected and uncorrected plots of energy loss vs. total energy

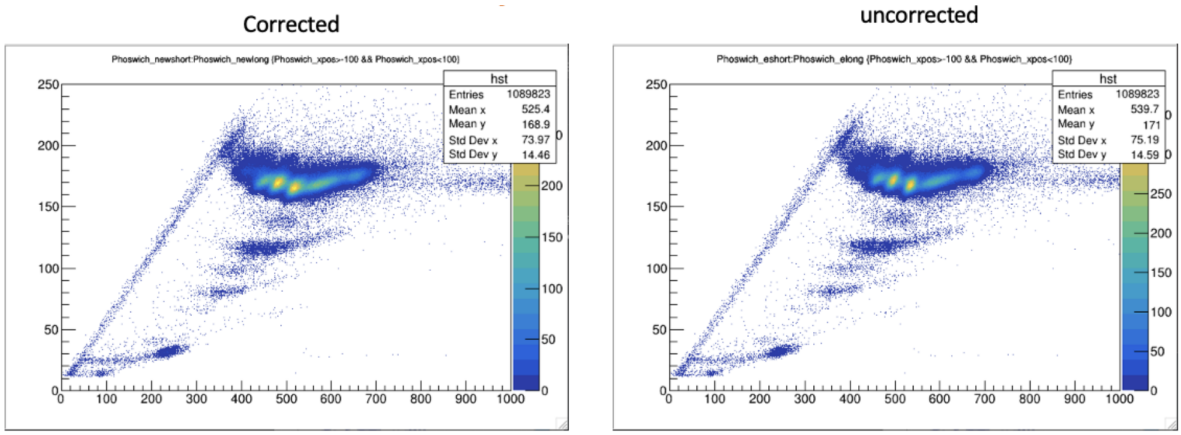

Figure 3.11: position corrected vs uncorrected for the production run, Using cubic spline method.

3.2 Particle Interaction Analysis & Scintillator Optimization

In order to model the expected energy deposited by various ion species in the thin and thick layers of the phoswich and deduce the corresponding loci in the ΔE vs. E plots, we utilized CATIMA. This computational tool, written in the C programming language, is an implementation of ATIMA (ATomic Interaction with MAtter), which is specifically designed for simulating and analyzing charged particle interactions with various target materials. Initially, we defined the materials' composition, density, and thickness, along with the type of charged particles involved in the experiment.

3.2.1 Birks' Formula

We incorporated Birks' formula into our analysis to account for the non-linear response of scintillators when charged particles pass through them, known as the scin-

tillator response function. This effect has to be corrected for to arrive at the true value of the energy deposited in the scintillators, as the non-linear dependence on the energy deposited can impact the overall accuracy of the experiment.

$$\frac{dL}{dx} = \frac{S\frac{dE}{dx}}{1 + k_B\frac{dE}{dx}} \tag{3.4}$$

Equation(3.4) is commonly referred to as Birks' formula. where $\frac{dL}{dx}$ is the scintillation light yield per unit path length, $\frac{dE}{dx}$ is the ionization energy loss per unit path length, S is a proportionality constant which is 1 in this case, and k_B is a constant related to ionization quenching which is around 1.26-2.07 x10^{-2} for polyvinyltoluene-based scintillators [16].

By examining the output data from CATIMA, along with the light output information derived from Birks' formula, we gained valuable insights into the behavior of charged particles within our experimental setup. The CATIMA models and Birks corrections were used to predict the ΔE vs. E curves for various ion species, which allowed us to determine the nuclides present in the data. This straightforward approach helped to enhance the accuracy and understanding of the processes involved in our experiment.

3.3 Calibration and Isotope Analysis: Comparing CATIMA and Production Run Data

By comparing the CATIMA calculations to the production run data, we identified discrepancies in the measured energy signals from the scintillators. To increase the accuracy of the measurements, this requires tuning the calibration of the detectors. We corrected for this using Short = Short + (F) * Long and Long = Long + Short, where F is a factor indicates the isotopes' best-fit curve.

After applying the correction, we were able to accurately determine the energy deposition of ions in the scintillators. This resulted in a more precise measurement of their energy and timing. By selecting an F value of 0.19 that best resembled the curvature of the isotopes, we successfully calibrated the signals and obtained reliable data.

In order to determine the range of energies for the various isotopes used in our experiment that could be successfully detected by the spectrometer, we employed the RAYTRACE code. By running RAYTRACE simulations and varying the input energy parameter, we identified the range of input energies that corresponded to ions hitting the scintillator, as shown in Table 3.2. This information was then used to restrict the energy ranges in our CATIMA simulations, ensuring that we only simulated particles that could physically reach the detector, thus accurately modeling the charged particle interactions.

Figure 3.12 demonstrates the successful agreement between CATIMA calculations and production run data, which validates our ability to separate and identify isotopes

Isotope	Min Energy (MeV)	Max Energy (MeV)
Ne17	770	840
Ne18	735	795
Ne19	700	690
Ne20	665	720
Ne21	635	690
Ne22	605	660
Ne23	580	630
O16	530	580
F19	570	615
O15	565	615
O14	605	655
O13	650	700
F18	600	650
F17	630	685
F16	670	725

Table 3.2: Energy limits for various isotopes

of neon, fluorine, and oxygen using our experimental setup. The agreement between calculations and data illustrates the effectiveness of our analysis methods. The successful identification of the Ne, F, and O nuclides confirms that the experiment can be performed as intended. In particular, the ability to make selections (gates) on these isotopes allows coincidences between states in ^{19}Ne and specific decay modes (alpha or gamma) to be deduced. This achievement underscores the potential of our study to contribute to a deeper understanding of nuclear reactions, decay processes, and atomic nuclei behavior.

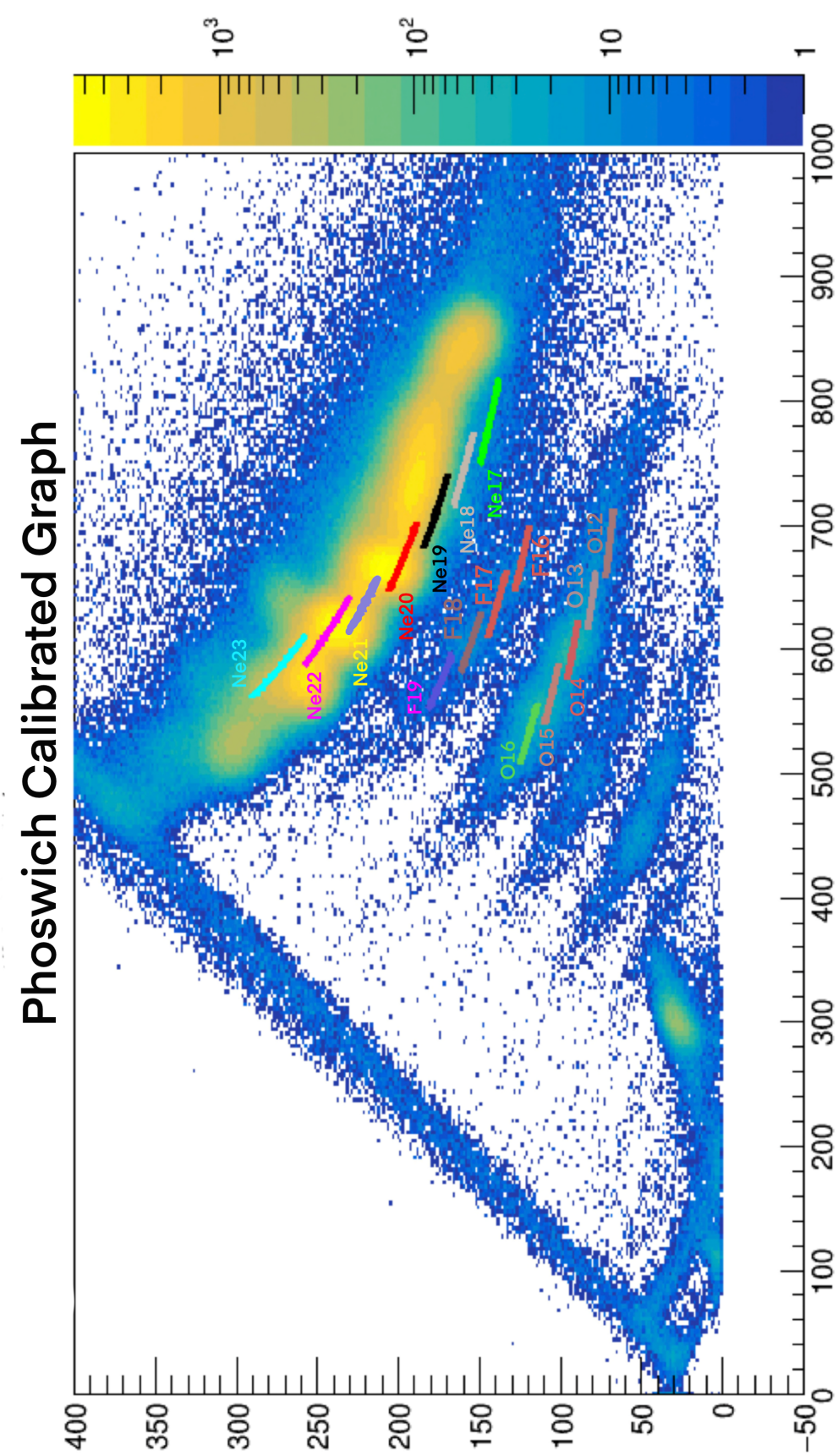

Figure 3.12: CATIMA calculations (colored lines) compared to the production run data for different isotopes. The plot shows the successful calibration of the detectors and highlights the energy and timing resolution achieved for these isotopes. The acceptable agreement between the calculations and experimental data validates our approach and confirms the accuracy of our measurements in the experiment.

Chapter 4

Conclusion

In conclusion, this experiment was designed to study the astrophysical rate of the $^{15}O(\alpha,\gamma)^{19}Ne$ reaction, a key factor in understanding the nucleosynthesis of heavy elements in the universe. By focusing on the measurement of this reaction via the $^{21}Ne(p, t)^{21}Ne$ reaction, we were able to investigate the branching ratios of alpha and gamma decays and determine the reaction rate.

The experiment involved several steps, including the use of CATIMA calculations for simulating charged particle interactions, detector calibration through the correction of measured phoswich signals for the overlap between signals produced in the thick and thin layers of the phoswich, and employing the RAYTRACE code to determine the energy ranges for various isotopes bent by the spectrometer into the detectors. These combined methodologies allowed for the successful identification of neon isotopes and the subsequent analysis of their decay processes.

The use of CATIMA calculations and RAYTRACE simulations allowed for the modeling of the expected energy loss and total energy signals of various ion species, thus verifying the isotope separation and identification in the data.

Our findings contribute to the successful implementation of particle identification in our experiment, a crucial aspect in the broader context of nuclear astrophysics. By ensuring accurate isotope separation and identification, this project lays the ground-

work for a more comprehensive understanding of nucleosynthesis and the production of heavy elements in the universe. These results have potential implications for various applications such as nuclear energy, medical imaging, and astrophysics, ultimately enhancing our understanding of the fundamental principles that govern atomic nuclei behavior.

Bibliography

[1] *Thermonuclear Reactions*, chapter 3, pages 147–217. John Wiley Sons, Ltd, 2007.

[2] R. H. Cyburt, A. M. Amthor, A. Heger, E. Johnson, L. Keek, Z. Meisel, H. Schatz, and K. Smith. Dependence of x-ray burst models on nuclear reaction rates. *The Astrophysical Journal*, 830(2):55, oct 2016.

[3] B. Davids, A. M. van den Berg, P. Dendooven, F. Fleurot, M. Hunyadi, M. A. de Huu, R. H. Siemssen, H. W. Wilschut, H. J. Wörtche, M. Hernanz, J. José, K. E. Rehm, A. H. Wuosmaa, and R. E. Segel. Astrophysical rate of $^{15}\mathrm{O}(\alpha,\gamma)^{19}\mathrm{Ne}$ via the (p,t) reaction in inverse kinematics. *Phys. Rev. C*, 67: 065808, Jun 2003.

[4] H. T. Fortune, H. Nann, and B. H. Wildenthal. Configuration of $^{19}\mathrm{Ne}(4.033, \frac{3}{2^+})$. *Phys. Rev. C*, 18:1563–1565, Oct 1978.

[5] G. Hackman, Sam M. Austin, T. Glasmacher, T. Aumann, B. A. Brown, R. W. Ibbotson, K. Miller, B. Pritychenko, L. A. Riley, B. Roeder, and E. Spears. Intermediate-energy coulomb excitation of $^{19}\mathrm{Ne}$. *Phys. Rev. C*, 61:052801, Apr 2000.

[6] Jordi José. Nucleosynthesis in stellar explosions: Type ia supernovae, classical novae, and type i x-ray bursts. *AIP Conference Proceedings*, 2076(1):030004, 2019.

[7] G.F. Knoll. *Radiation Detection and Measurement*. Wiley, 2010.

[8] A. M. Laird, S. Cherubini, A. N. Ostrowski, M. Aliotta, T. Davinson, A. Di Pietro, P. Figuera, W. Galster, J. S. Graulich, D. Groombridge, J. Hinnefeld, M. Lattuada, P. Leleux, L. Michel, A. Musumarra, A. Ninane, M. G. Pellegriti, A. C. Shotter, Spitaleri, A. Tumino, J. Vervier, and P. Woods. Indirect study of the astrophysically important $^{15}\mathrm{O}(\alpha,\gamma)^{19}\mathrm{Ne}$ reaction through $^{2}\mathrm{H}(^{18}\mathrm{Ne},^{19}\mathrm{Ne})^{1}\mathrm{H}$. *Phys. Rev. C*, 66:048801, Oct 2002.

[9] H.K.W. Leegte, E.E. Koldenhof, A.L. Boonstra, and H.W. Wilschut. Calibration of phoswich detectors. *Nuclear Instruments and Methods in Physics Research Section A: Accelerators, Spectrometers, Detectors and Associated Equipment*, 313 (1):26–30, 1992.

[10] P.V. Magnus, M.S. Smith, A.J. Howard, P.D. Parker, and A.E. Champagne. Measurement of $^{15}\mathrm{o}(\alpha,\gamma)^{19}\mathrm{ne}$ resonance strengths. *Nuclear Physics A*, 506(2): 332–345, 1990.

[11] T. Nikšić, D. Vretenar, and P. Ring. Relativistic random-phase approximation with density-dependent meson-nucleon couplings. *Phys. Rev. C*, 66:064302, Dec 2002.

[12] D.M. Pringle, W.N. Catford, J.S. Winfield, D.G. Lewis, N.A. Jelley, K.W. Allen, and J.H. Coupland. The oxford mdm-2 magnetic spectrometer. *Nuclear Instruments and Methods in Physics Research Section A: Accelerators, Spectrometers, Detectors and Associated Equipment*, 245(2):230–247, 1986.

[13] D.M. Pringle and W.J. Vermehr. Alpha-particle decay widths of levels in 19f. *Nuclear Physics A*, 499(1):117–130, 1989.

[14] W. P. Tan, J. L. Fisker, J. Görres, M. Couder, and M. Wiescher. $^{15}\mathrm{O}(\alpha,\gamma)^{19}\mathrm{Ne}$ breakout reaction and impact on x-ray bursts. *Phys. Rev. Lett.*, 98:242503, Jun 2007.

[15] D.R. Tilley, H.R. Weller, C.M. Cheves, and R.M. Chasteler. Energy levels of light nuclei a = 18–19. *Nuclear Physics A*, 595(1):1–170, 1995.

[16] L. Torrisi. Plastic scintillator investigations for relative dosimetry in proton-therapy. *Nuclear Instruments and Methods in Physics Research Section B: Beam Interactions with Materials and Atoms*, 170(3):523–530, 2000.